HYDROLOGICAL PROCESSES
Hydrol. Process. **30**, 3804–3823 (2016)
Published online 15 June 2016 in Wiley Online Library
(wileyonlinelibrary.com) DOI: 10.1002/hyp.10893

Spatio-temporal variability of water and energy fluxes – a case study for a mesoscale catchment in pre-alpine environment

Luitpold Hingerl,[1]* Harald Kunstmann,[1,2] Sven Wagner,[1,2] Matthias Mauder,[2] Jan Bliefernicht[1] and Riccardo Rigon[3]

[1] *Institute of Geography, University of Augsburg, Augsburg, Germany*
[2] *Institute of Meteorology and Climate Research (IMK-IFU), Karlsruhe Institute of Technology (KIT), Garmisch-Partenkirchen, Germany*
[3] *Department of Civil and Environmental Engineering, CUDAM, University of Trento, Trento, Italy*

Abstract:

Water and energy fluxes at and between the land surface, the subsurface and the atmosphere are inextricably linked over all spatio-temporal scales. Our research focuses on the joint analysis of both water and energy fluxes in a pre-alpine catchment (55 km^2) in southern Germany, which is part of the Terrestrial Environmental Observatories (TERENO). We use a novel three-dimensional, physically based and distributed modelling approach to reproduce both observed streamflow as an integral measure for water fluxes and heat flux and soil temperature measurements at an observation location over a period of 2 years. While heat fluxes are often used for comparison of the simulations of one-dimensional land surface models, they are rarely used for additional validation of physically based and distributed hydrological modelling approaches. The spatio-temporal variability of the water and energy balance components and their partitioning for dominant land use types of the study region are investigated. The model shows good performance for simulating daily streamflow (Nash–Sutcliffe efficiency > 0.75). Albeit only streamflow measurements are used for calibration, the simulations of hourly heat fluxes and soil temperatures at the observation site also show a good performance, particularly during summer. A limitation of the model is the simulation of temperature-driven heat fluxes during winter, when the soil is covered by snow. An analysis of the simulated spatial fields reveals heat flux patterns that reflect the distribution of the land use and soil types of the catchment. The water and energy partitioning is characterized by a strong seasonal cycle and shows clear differences between the selected land use types. Copyright © 2016 The Authors Hydrological Processes Published by John Wiley & Sons Ltd.

KEY WORDS water and energy flux analysis; eddy covariance measurements; GEOtop; Terrestrial Environmental Observatories (TERENO)

Received 19 June 2015; Accepted 13 April 2016

INTRODUCTION

The spatial and temporal variability of water on the land surface is a crucial factor for the development of ecosystems. Once water reaches the earth's surface as precipitation, its dynamic redistribution is controlled by surface and subsurface characteristics, by atmospheric conditions and by the available amount of incident solar energy. Assessments of the intertwined water and energy cycle were carried out, e.g. within the framework of the Global Energy and Water Cycle Experiment (Chahine and Vane, 1995; Lawford *et al*., 2007). Its aim was to better understand and quantify hydrological processes on the global scale and the interactions between the atmosphere, the land surface and the ocean. At smaller spatio-temporal scales, the effect of land–atmosphere interactions and the impact of land use change on water and energy fluxes have been analysed and reviewed (e.g. by Betts *et al*., 1996; Pielke *et al*., 1998; Seneviratne *et al*., 2006; Roy *et al*., 2007; Seneviratne *et al*., 2010; Pielke *et al*., 2011; Betts *et al*., 2013; Arnault *et al*., 2015). Water and energy balances of a specific location or a river basin are influenced by various factors, but particularly by the composition and structure of the vegetation (Foley *et al*., 2000; Bonan, 2008; Pielke *et al*., 2011), the soil type (Pielke *et al*., 1998) and land use and land management practices (Bonan, 2008; Dirmeyer *et al*., 2010). These factors considerably modify state variables of the land surface (e.g. soil moisture and soil temperature) and land–atmosphere exchange processes (e.g. evapotranspiration or sensible heat fluxes) and have a direct impact on the evolution of the atmospheric boundary layer (Wang and Eltahir, 2000; Bonan, 2008).

*Correspondence to: Harald Kunstmann, Karlsruhe Institute of Technology, Kreuzeckbahnstr. 19, 82467 Garmisch-Partenkirchen, Germany.
E-mail: harald.kunstmann@kit.edu

It is land surface models such as the Noah land surface model (Chen and Dudhia, 2001) that account for both the intertwined water and energy fluxes. Overgaard *et al.* (2005) called these types of land surface models energy-based land surface models. These energy-based land surface models are typically used as lower boundary conditions in regional climate models, describing the one-dimensional vertical transfer of water and energy between the soil, the vegetation and the atmosphere. Pure energy-based land surface models have been extended within the last years using biochemical process formulations to include vegetation dynamics and carbon exchange processes (Pitman, 2003). Recent overviews are given, e.g. by Prentice *et al.* (2015) and Zhao and Li (2015). Model examples are the Community Land Model (Dai *et al.*, 2003; Lawrence *et al.*, 2011), the multi-physics version of the Noah land surface model (Niu *et al.*, 2011; Yang *et al.*, 2011) and the Joint UK Land Environment Simulator (Best *et al.*, 2011; Clark *et al.*, 2011). Further model developments are presented by Montaldo *et al.* (2005) and Drewry *et al.* (2010).

However, a detailed treatment of lateral water fluxes such as surface runoff is usually not performed within these types of land surface models. The consideration of lateral fluxes is the focus of distributed hydrological models: they have been designed for a three-dimensional simulation of subsurface and surface water fluxes within a hydrological basin of interest to take into account the spatial heterogeneity of a catchment. Prominent examples are the physically based models SHE (Abbott *et al.*, 1986) and its extensions such as MIKE-SHE (Refshaard *et al.*, 1995; Graham and Butts, 2005). Further physical-based examples are Topographic Kinematic Approximation and Integration (Ciarapica and Todini, 2002), Lisflood (De Roo *et al.*, 2000; Van Der Knijff *et al.*, 2010) or WaSiM (Schulla and Jasper, 2015).

However, a detailed treatment of energy fluxes like in energy-based land surface models is usually not performed within these distributed hydrological models (Overgaard *et al.*, 2005). Distributed hydrological models usually approximate or even lack a consistent intertwined description of water and energy fluxes. To combine the processes presented by energy-based land surface models and physically based distributed hydrological models, various hydrological models have been proposed based on an improved intertwined description of water and energy fluxes. These models are usually named as water and energy balance models (Famiglietti and Wood, 1994; Singh and Frevert, 2010) or distributed land surface models (Overgaard *et al.*, 2005). Model examples are VIC (Liang *et al.*, 1994; Gao *et al.*, 2010), GEOtop (Rigon *et al.*, 2006) and its extensions (e.g. Endrizzi *et al.*, 2014), the Noah Distributed Hydrological Modeling System (NDHMS, Gochis *et al.*, 2013), tRIPS (Ivanov *et al.*, 2004; Vivoni *et al.*, 2007), the Distributed Hydrology–Soil–Vegetation Model (Wigmosta *et al.*, 2002; Cuo *et al.*, 2008) and the recent version of MIKE-SHE in combination with an energy-based land surface model (Larsen *et al.*, 2014). Distributed hydrological models have been also extended by biochemical process formulations to study the impact of hydrological processes on bio-geochemical processes and their interactions within a river basin (Newman *et al.*, 2006). These models are often named as eco-hydrological models. The need for these models was already noted by Rodriguez-Iturbe (2000). An overview about eco-hydrological modelling is given by Krysanova and Arnold (2008) focusing on the Soil Water Assessment Tool (Arnold *et al.*, 1998) and the Regional Hydro-Ecologic Simulation System (e.g. Band, 1993; Tague and Band, 2004). During the last years, several further eco-hydrological models have been developed and evaluated for specific river basins (Ivanov *et al.*, 2008a; Fatichi *et al.*, 2012; Shen *et al.*, 2013; Niu *et al.*, 2014).

Beside the integration of biochemical process formulations within the distributed hydrological models, the improvement of the representation of additional hydrological processes played a further important role. For example, Maxwell and Kollet (2008) and Kollet and Maxwell (2008) combined a groundwater model with an integrated surface runoff module (ParFlow) and the energy-based land surface model Community Land Model to study the influence of groundwater dynamics on energy fluxes at the land surface.

To evaluate the performance of water and energy balance models, the simulation results of these models are usually compared with discharge measurements. In selected cases, remote sensing information is used, e.g. for a spatial validation of evapotranspiration, soil moisture and soil temperature simulations. Few studies also integrated water and energy flux measurements of micrometeorological stations based on eddy covariance (EC) techniques (e.g. Rigon *et al.*, 2006) for model validation. EC stations have been continuously established in various terrestrial ecosystems worldwide (e.g. Baldocchi *et al.*, 2001; Wilson *et al.*, 2002; Zacharias *et al.*, 2011; Bliefernicht *et al.*, 2013) providing continuous sub-hourly information of water and energy fluxes and further variables. EC information is a primary source for calibration and validation of land surface models (e.g. Hogue *et al.*, 2005; Abramowitz *et al.*, 2008; Drewry *et al.*, 2010; Rosero *et al.*, 2010; Niu *et al.*, 2011) and allow additional information for a comparison of simulation results from climate simulations (e.g. Decker *et al.*, 2012). Recently, a number of mesoscale compartment crossing hydrometeorological observatories have been established (e.g. Zacharias *et al.*, 2011; Grant *et al.*, 2012), providing a comprehensive set of additional

measurement variables for an in-depth analysis of environmental processes and evaluation of physical-based models developed in hydrology, meteorology and further disciplines.

Within this research of water and energy flux modelling and observation at various temporal and spatial scales, our study aims at being a further step towards the required co-evolution of advanced physically based distributed hydrological models and hydrometeorological observatories like Terrestrial Environmental Observatories (TERENO). The specific objective of this study is to investigate whether a water and energy balance model is able to achieve a reasonable performance in reproducing spatio-temporal patterns of water and energy fluxes within a hydrological basin, if only discharge measurements at the basin outlet are used for calibration. By considering only streamflow measurements for calibration, we mimic the traditional way of calibrating hydrological models. The simulated water and energy fluxes are then jointly analysed and compared with both discharge and EC flux measurements. EC measurements are often used for the validation of land surface models, but their consideration in distributed hydrological models is only rarely performed. If EC data are used in distributed hydrological modelling, validation is performed mostly on an event basis, e.g. for a flood event or a rather short period of several months (Chen *et al.*, 2005; Rigon *et al.*, 2006; Ivanov *et al.*, 2008b; Vivoni *et al.*, 2010).

In our study, we present a comparison of the simulated water and energy fluxes with EC measurements over a period of 2 years. This allows an in-depth evaluation of the model performance for different hydrological conditions during these 2 years. The simulations are performed and evaluated on an hourly basis. We also perform an in-depth assessment of the simulated patterns of the water and energy fluxes on different temporal and spatial scales and their partitioning for selected land use types and soil types. The study is performed for a heterogeneous, small mesoscale catchment located in a pre-alpine region of Southern Germany using GEOtop 1.45. The comparison of the simulated water and energy fluxes is performed using a set of hourly discharge measurements and micrometeorological measurements provided by an EC station, which is established within the framework of the TERENO initiative (Zacharias *et al.*, 2011) for the TERENO pre-alpine test site.

STUDY SITE DESCRIPTION AND OBSERVATIONAL DATA SETS

Meteorological and catchment characteristics

The study region is the catchment of the river Rott with an area of 55 km^2. It is located in the Danube basin in the pre-alpine region of Southern Germany (Figure 1). The catchment is equipped with a discharge station at the outlet of the catchment with a mean discharge of 0.86 $m^3 s^{-1}$. Meteorological observations are taken from three stations operated by the German weather service with hourly measurements for precipitation, air temperature, relative humidity and wind speed. Micrometeorological measurements are obtained by an EC station

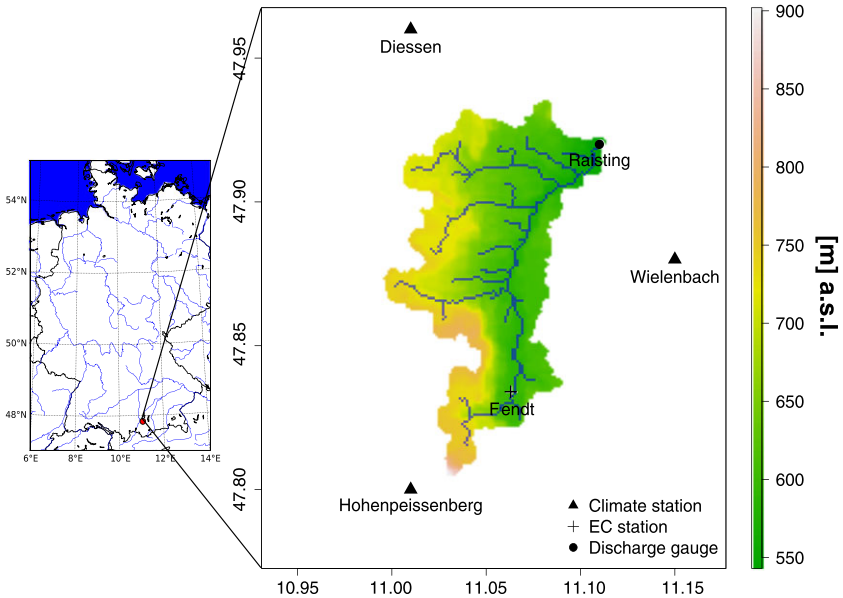

Figure 1. The Rott catchment in the pre-alpine region of Germany and the positions of the discharge gauge Raisting, the Terrestrial Environmental Observatories test site Fendt with the micrometeorological stations using an eddy variance technique, the river network and the meteorological stations used for the meteorological forcing of the model

(Mauder *et al*., 2013). It is located inside the catchment, providing continuous sub-hourly measurements since 2010 for all meteorological variables (precipitation, air temperature, relative humidity, wind speed, air pressure, global shortwave radiation, diffuse shortwave radiation, net shortwave radiation and incoming longwave radiation). Hourly measurements of soil temperature as well as soil, sensible and latent heat fluxes are taken from the EC station, enabling an energy flux evaluation of the model simulations.

The mean annual precipitation amount of the study region is 1130 mm with an annual mean temperature of 6.9 °C and an average of 73 days with a snow thickness of more than 10 cm (calculated for the period from 1960 to 2010). The dominant soil types of the study region are *Lessive* (76%), *Cambisol* (13%) and *Histosol* (9%) according to the soil classification system of the World Reference Base for Soil Resources (FAO *et al*., 1998) (Figure 2a). The predominant land use types are *pasture* (44%), as well as *coniferous* (37%, mainly spruces) and *mixed forests* (18%, mainly beeches) according to the soil cover data obtained by the Coordination of Information on the Environment project (www.corine.dfd.dlr.de). Smaller areas are occupied by *villages* (2%) as well as some *peat* (0.8%) and *marsh land* (0.5%) south of the lake *Zellsee* (Figure 2b).

Description of micrometeorological measurements

The EC station is part of the TERENO pre-alpine observatory and located near the village of Fendt (e.g. Eder *et al*., 2014). The vegetation cover of the EC site is intensively managed grassland. Sensible and latent heat fluxes are based on wind, temperature and humidity measurements performed at 3.5-m height using a sonic anemometer–thermometer and an open-path infrared gas analyser. Radiation components are measured at 2 m using a net radiometer. The heat flux is measured at a soil depth of 0.08 m. Soil temperatures used in this study are based on measurements taken at 0.02, 0.06, 0.12, 0.25, 0.35 and 0.5 m. The statistical post-processing of the EC data was performed in accordance with Mauder *et al*. (2013) using the software TK3 (Mauder and Foken, 2015).

To assess the quality of the EC measurements in terms of the energy balance closure, the sum of the hourly sensible and latent heat fluxes are compared with the available energy at the surface, which is the net radiation minus the heat flux. This relationship is illustrated in Figure 3 for the hydrological year 2011 (November 2010–October 2011). A perfect match is illustrated when all data pairs follow the diagonal of the diagram. The correspondence between the heat fluxes and the available energy at the surface is quite high as expressed by the coefficient of determination ($R^2 = 0.89$). However, following Mauder *et al*. (2006), a slope of 0.62 of the regression line reveals a gap in the energy balance of approximately 38%. It is known that *in situ* surface flux measurements based on EC techniques can show a significant lack of energy balance closure (Stoy *et al*., 2013). Possible reasons for this gap are object of intense investigations in micrometeorological research. According to Foken *et al*. (2010), the non-closure of the energy balance is a scale problem as tower-based EC measurements can only capture small-scale fluxes. The energy loss is attributed to large-scale eddies that can only be captured on the landscape scale, for instance with scintillometers or airborne sensors. Hence, a poor energy balance closure cannot be interpreted as an indication of poor data quality of the measured fluxes. Another possible explanation is the insufficient consideration of

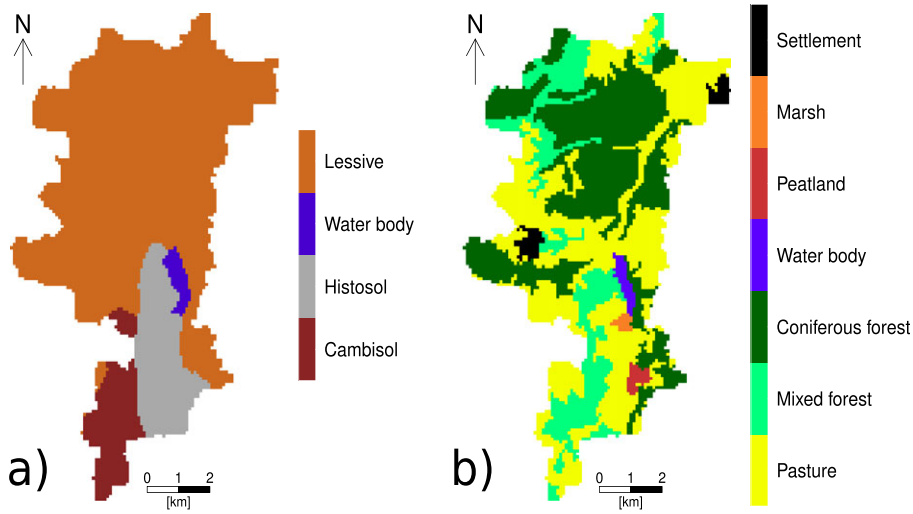

Figure 2. Soil (a) and land use (b) classification of the Rott catchment

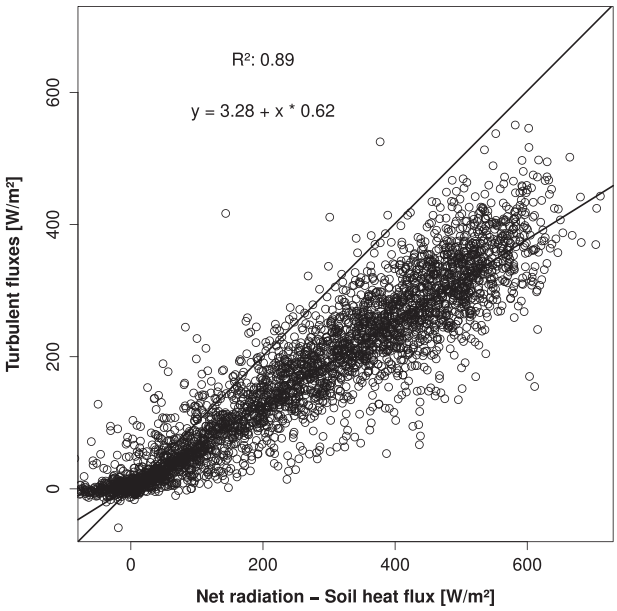

Figure 3. Sum of turbulent hourly heat fluxes *versus* available energy at the surface from measurements at the Terrestrial Environmental Observatories test site Fendt during the hydrologic year 2011

heat stored in soil and biomass (Lindroth *et al*., 2010). However, the ground heat flux data already include the soil heat storage, and the storage change in the biomass is probably small because of the short-statured vegetation. Therefore, heat storage can be considered of minor relevance for this study site.

MODELLING DISTRIBUTED WATER AND ENERGY FLUXES USING GEOTOP

Basic description of GEOtop

GEOtop is a high-resolution distributed water and energy budget simulation model developed for applications in small catchments in complex terrain (Bertoldi *et al*., 2004; Rigon *et al*., 2006; Endrizzi *et al*., 2014). It is designed for simulating the water and energy cycle in continuum and for calculating the discharge like a classic rainfall–runoff model as well as surface and subsurface flows and the water content of the soil in the saturated and unsaturated zones. In the coupled numerical solution of the heat and water flow equations for three-dimensional grid boxes, the influence of vegetation (Endrizzi and Marsh, 2010) as well as snow cover and snow melt is included (Zanotti *et al*., 2004). This study uses the GEOtop model version 1.45. It is an extension of GEOtop version 0.75 presented by Rigon *et al*. (2006) and Bertoldi *et al*. (2006) and is similar to GEOtop version 2 that was recently released by Endrizzi *et al*. (2014). An application of GEOtop 2 is given by Bertoldi *et al*. (2014) using the simulated soil moisture fields for an additional comparison of soil moisture patterns derived from satellite images. More details on process formulations used in this model version are given in the appendix, also including a description of the relevant parameters that are applied for model calibration. Further model developments and evaluation studies of GEOtop comprise the simulation of soil moisture (Gebremichael *et al*., 2009), land surface temperature (Bertoldi *et al*., 2010) and ground temperature (Gubler *et al*., 2013).

Generation of spatially distributed model input data

The spatial distribution of the hourly meteorological observations over the entire catchment area is obtained by using ordinary kriging (Kitanidis, 1997) for precipitation, a height-dependent interpolation method for air temperature after Brutsaert (1982) and air pressure and an interpolation method for radiation considering shadowing effects by the terrain and changing absorbency at different elevations (Formetta *et al*., 2013). The catchment boundaries and the terrain-dependent parameters drainage direction, river network, slope and aspect are calculated using the Udig Spatial Toolbox (Abera *et al*., 2014) based on techniques described by Rodriguez-Iturbe and Rinaldo (1997) and Rigon *et al*. (2006). As input information, the digital elevation model from the Shuttle Radar Topographic Mission carried out by NASA (Consultative Group on International Agricultural Research–Consortium for Spatial Information: http://srtm.csi.cgiar.org/) is used. The spatial distribution of the soil types given in Figure 2 is based on the *Bodenuebersichtskarte der Bundesrepublik Deutschland* with a resolution of approximately 2 km. The land use and soil maps are adjusted to the catchment area and interpolated to the 90-m resolution of the digital elevation model. Soil hydraulic properties are adopted from previous modelling studies in this region (Kunstmann *et al*., 2006; Smiatek *et al*., 2012; Ott *et al*., 2013). The model domain extends till 10-m depth and is partitioned into seven soil layers with increasing thickness from the surface to bottom layers. The integration interval of the model is 1 h. The model parameters for the various land cover types of the Rott catchment are listed in Table I.

Model calibration and validation procedure

The model calibration is carried out for the period November 2009 till October 2010, using only hourly discharge measurements from the gauge at the basin outlet (Figure 1). In this study, we explore the quality of this standard calibration approach for the simulation of the heat fluxes. The dynamics of discharge is comparatively low and takes place on a much larger scale in comparison with the turbulent heat fluxes measured at

Table I. Model parameters for the different land cover types.

Parameter	Pasture	Coniferous forest	Mixed forest	Marsh	Peatland	Settlement
Vegetation height (mm)	400	2500	3000	400	40	40
Leaf area index (—)	4	8	10	4	4	0.1
Canopy fraction (—)	0.9	1	1	0.9	0.9	0.1
Root depth (mm)	50	1300	1400	100	100	50
Minimum stomatal resistance ($s\,m^{-1}$)	60	60	65	30	30	60
Vegetation albedo (—)	0.1	0.1	0.1	0.1	0.1	0.1
Ground albedo (—)	0.15	0.15	0.15	0.15	0.15	0.15

the EC station. But its characteristics constitute an integral response of the catchment. Discharge serves as a quality criterion of the sum of interacting processes in influencing the spatial and temporal dynamics of water at the surface of the earth. Based on a reference set-up using the soil parameter values of previous modelling studies in the investigation area with the model WaSiM (Kunstmann *et al*., 2004, 2006), the following four parameters are calibrated step by step: the horizontal and vertical saturated hydraulic conductivity k_h and k_v, the surface roughness length outside the channel C_m, and the van Genuchten parameter α. In the first iteration step, α is reduced successively within the interval ranging from 0.99 to 0.01 using a step size of 0.01 to increase the soil suction. In a second step, k_v and k_h are increased and decreased simultaneously and apart from each other within the interval 0.99–0.03 with a step size of 0.08. Based on the parameters with the best fitting between simulated and measured discharges, this step is repeated but with a finer step size. In the last step of the iteration, the roughness C_m is calibrated. As its sensitivity is comparatively low, the same value of C_m was assumed for all land use types. The adjustment of all parameters during the calibration process was accomplished in each iteration step for every soil layer and every soil type simultaneously and by the same factor to keep the specific characteristics of the soil types. The final model parameters of the calibration procedure are listed in Table II. The value of the final roughness parameter C_m is 0.5.

The validation of the model is performed for a period ranging from November 2010 to October 2011 using daily and hourly discharge measurements at the catchment outlet and hourly heat fluxes and soil temperature measurements at the EC station. For the discharge simulations, the model performance is evaluated using the Nash–Sutcliffe efficiency (NSE) coefficient (Nash and Sutcliffe, 1970). As the NSE overstates the quality of the highest peaks compared with low-flow periods, the logarithmic NSE is calculated based on the logarithm of the discharge values. Congruency in the dynamics of simulated and measured discharges regardless of their absolute values is analysed using the coefficient of determination R^2 (e.g. Bahrenberg *et al*., 1992). In addition, the bias of the discharge simulations is analysed.

COMPARISON WITH DISCHARGE AND EC MEASUREMENTS

Discharge measurements

In Figure 4, the simulated and measured hydrographs at the gauge at Raisting for the calibration period are displayed for the daily discharge. As a result of the described calibration procedure, an NSE of 0.75 for daily discharge and 0.64 for hourly discharge could be achieved, indicating a reasonable congruency of simulated and measured discharge peaks. With respect to the simulated discharge dynamics, an R^2 of 0.78 on a daily

Table II. Calibrated soil parameter values for all soil types.

Soil layer	*Cambisol*			*Lessive*			*Histosol*		
	k_h ($mm\,s^{-1}$)	k_v ($mm\,s^{-1}$)	α (mm^{-1})	k_h ($mm\,s^{-1}$)	k_v ($mm\,s^{-1}$)	α (mm^{-1})	k_h ($mm\,s^{-1}$)	k_v ($mm\,s^{-1}$)	α (mm^{-1})
1	1	1	0.0005833	1	1	0.000625	1	1	0.00033
2	0.0044	0.4	0.0005833	0.0011	0.1	0.000625	0.00889	0.8	0.00033
3	0.0011	0.1	0.000625	0.0011	0.1	0.000625	0.00889	0.8	0.00033
4	0.0011	0.1	0.000625	0.00078	0.07	0.0001583	0.00011	0.01	0.000167
5	0.00033	0.03	0.0004	0.00078	0.07	0.0001583	0.00011	0.01	0.000167
6	0.00033	0.03	0.0004	0.00033	0.03	0.0001583	0.0022	0.2	0.000625
7	0.00033	0.03	0.0004	0.00033	0.03	0.0001583	0.0022	0.2	0.000625

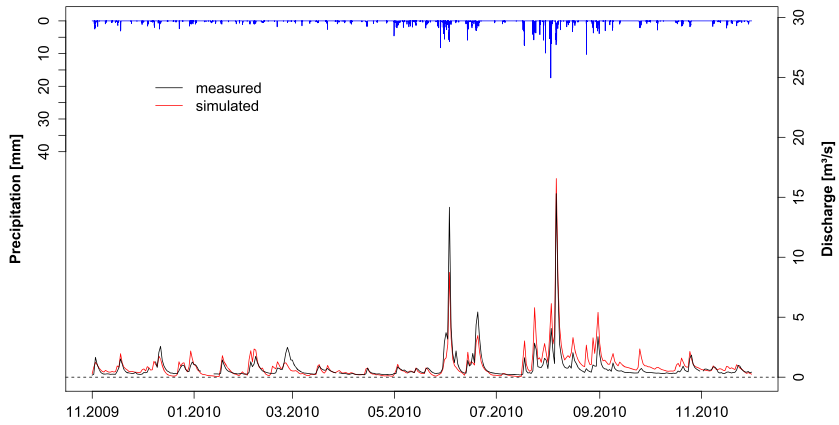

Figure 4. Simulated and measured daily discharge values at the gauge Raisting for the calibration period with a Nash–Sutcliffe efficiency (NSE) of 0.75, a logarithmic NSE of 0.34 and an R^2 of 0.78. In addition, the hourly areal precipitation is given for the Rott catchment

scale and 0.8 on an hourly scale could be obtained. The total simulated discharge volume for the hydrologic year 2010 sums up to 9419 m^3, showing an overestimation of approximately 37% compared with the measured discharge volume of 6869 m^3. This overestimation of the yearly discharge volume is mainly the result of an overestimation of the low-flow periods during summer and autumn when baseflow dominates. The logarithmic NSE with a value of 0.34 for daily discharge and 0.22 for hourly discharge shows a reasonable, but clearly smaller, model performance for reproducing the rising and recessing limbs of the flood peaks.

Figure 5 shows a comparison of simulated and measured mean daily discharge values for the validation period, with a similar performance as in the calibration period indicated by an NSE of 0.75. With respect to the rising limbs and the tails of the peaks, as well as the dynamics, a logarithmic NSE of 0.35 and an R^2 of 0.81, respectively, indicate a slightly better agreement between simulations and measurements for the validation period. As in the calibration period, the simulations tend to overestimate the discharge peaks especially in the summertime. An increase in amount and intensity of precipitation during the summer months leads to an oversaturation of the soil and consequently larger amount of Dunnian-type runoff and therefore higher flood peaks than in winter and spring. The underestimation of the two peaks in January and at the beginning of June can be due to insufficient accuracy in the precipitation measurement uncertainties regarding the applied interpolation method, and further uncertainties like the simulation of the snowline within the model. For the validation period of the hydrologic year 2011, total simulated discharge has a volume of 9822 m^3 overestimating the observed volume 7321 m^3 by around 25%. Again, this overestimation of the yearly discharge volume is primarily due to the overestimation of the low-flow periods during the summer and autumn when the discharge is dominated by the baseflow.

Hourly heat fluxes and soil temperature

In Figure 6, hourly values of the simulated sensible, latent and soil heat flux are compared with the measure-

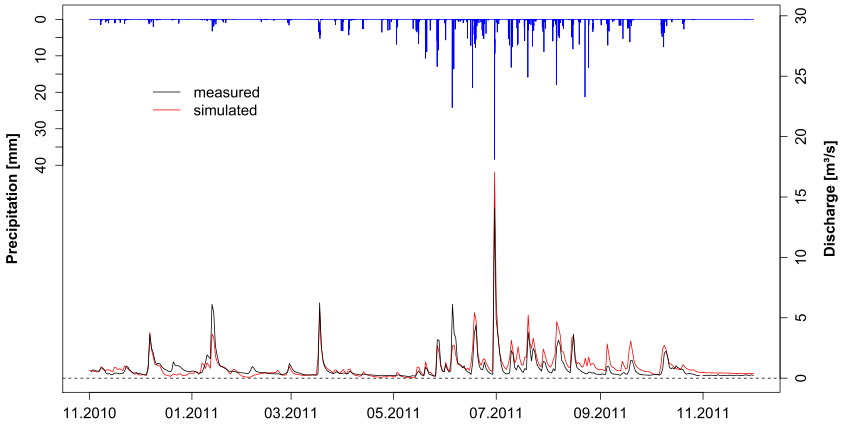

Figure 5. Simulated and measured daily discharge at the gauge Raisting for the validation period with a Nash–Sutcliffe efficiency (NSE) of 0.75, a logarithmic NSE of 0.35 and an R^2 of 0.81. In addition, the hourly areal precipitation is given for the Rott catchment

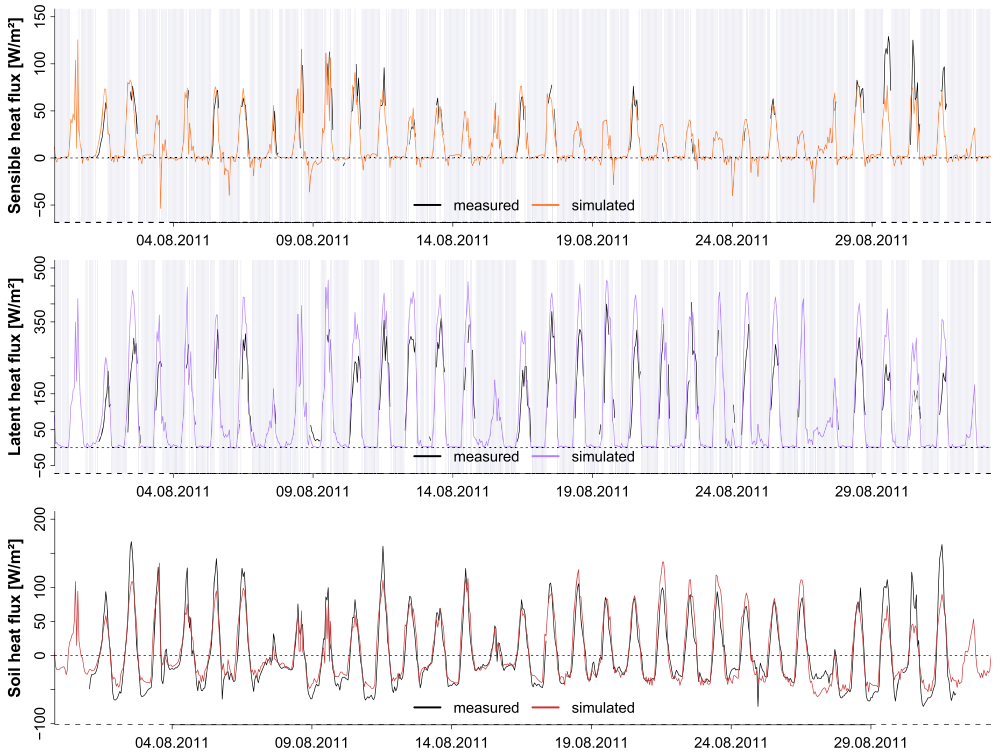

Figure 6. A sequence of simulated and observed hourly sensible, latent and soil heat fluxes for the validation period in August 2011 at the eddy covariance station Fendt. Grey bars indicate periods where a statistical quality criterion based on the occurrences of turbulence in the atmosphere is not fulfilled

ments of the EC station for August 2011. The grey bars within the plots of latent and sensible heat fluxes indicate periods where a quality criterion testing the underlying assumptions of the EC method is not fulfilled (Foken *et al*., 2005). Most of the reliable measurements can be found during the day when convection generates turbulence and the energy exchange between the earth surface and the atmosphere reaches its maximum intensity.

All three fluxes are reproduced fairly well by the model, except systematically larger simulated midday maxima of the latent heat fluxes compared with the observations. These may be due to a lack of energy balance closure of the measurements (38%) as illustrated in Figure 3 on the one hand and to a high soil water content in the simulations on the other hand. As a result, the specific heat of the soil matrix is too high, leading to an underestimation of the sensible and soil heat fluxes. This becomes apparent in Figure 7 and in Table III where simulated and measured heat fluxes are compared for different seasons.

The concentration of a wide range of simulated soil heat flux values with a corresponding small range of slightly negative measured values around a vertical line during winter is due to negative measurements without a strong daily cycle when the soil surface is covered by snow. This effect, however, is not reproduced by simulations that have a larger standard deviation (s_{sim}) than observations (s_{obs}), leading to very low temperatures following the dynamics of the air temperature (Table III). All three fluxes show consequently low congruency in winter with an R^2 of 0.17 for soil heat flux, 0.04 for sensible heat flux and 0.15 for latent heat flux. The best simulation results could be achieved in summer. In the case of the soil heat flux (Figure 7a), the scattering of data pairs around the ideal line is clearly lower in autumn ($R^2 = 0.60$) as well as in spring and summer ($R^2 = 0.71$) than in winter ($R^2 = 0.17$). The broadest scattering around the regression line can be observed for the sensible heat flux, which also shows the lowest fit in all seasons.

The comparison of measured and simulated latent heat in Figure 7 shows a clear but reasonable scattering in autumn, spring and summer with an R^2 of 0.72, 0.74 and 0.80, respectively. The cumulative occurrence of very low simulated values with corresponding high measurements at the bottom of the charts is probably caused by an underestimation of turbulence in the nocturnal atmospheric boundary layer as a result of the calculation of the bulk coefficient C. Figure 8 finally shows soil temperature simulations in comparison with the measurements for different depths indicating a slight underestimation of the simulated temperature for the winter period.

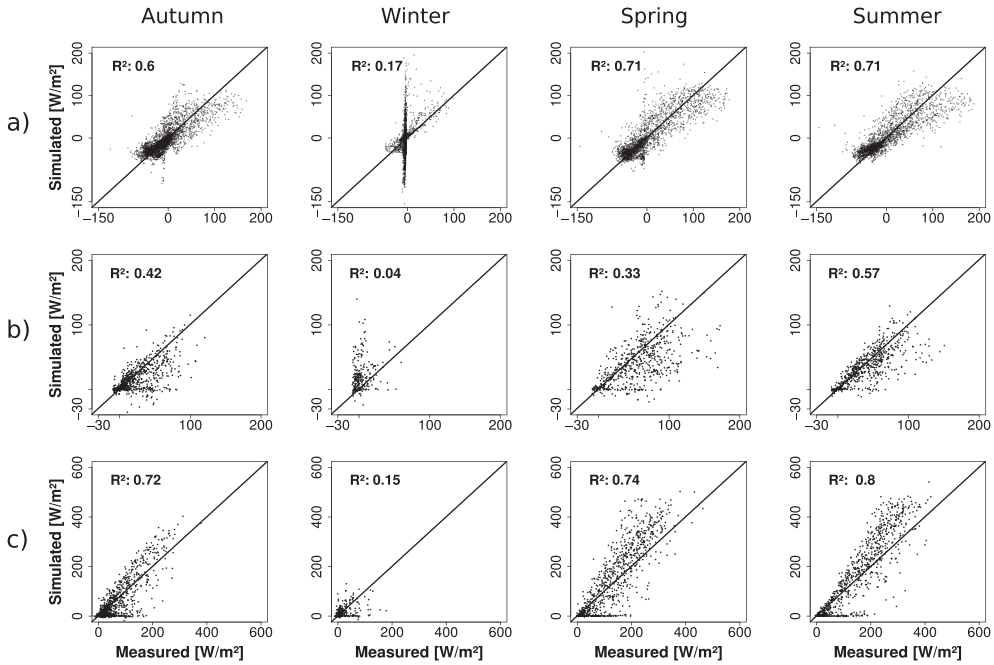

Figure 7. Measured against simulated (a) soil, (b) sensible and (c) latent heat fluxes subdivided into the four seasons of the validation period, the hydrological year Nov. 2010–Oct. 2011

Table III. Mean absolute error (MAE), standard deviation (s_{obs} and s_{sim}), mean ($\bar{x}_{obs}$ and $\bar{x}_{sim}$) and R^2 for simulated and observed sensible (H), latent (λE) and soil (G) heat fluxes subdivided into the four seasons of the validation period.

	H (W m^{-2})				λE (W m^{-2})				G (W m^{-2})			
	SON	DJF	MAM	JJA	SON	DJF	MAM	JJA	SON	DJF	MAM	JJA
MAE	14	21	25	14	33	17	57	57	18	39	20	19
s_{obs}	24	12	36	31	72	29	95	105	39	15	53	51
s_{sim}	20	23	33	27	92	23	140	150	38	95	49	42
$\bar{x}_{obs}$	24	3	56	42	74	20	135	155	−4	−3	5	3
$\bar{x}_{sim}$	17	21	42	36	67	16	154	176	−5	−5	6	5
R^2 (—)	0.42	0.04	0.33	0.57	0.72	0.15	0.74	0.8	0.6	0.17	0.71	0.71

SPATIO-TEMPORAL PATTERNS OF SELECTED WATER AND ENERGY BALANCE COMPONENTS

The monthly water and energy balances averaged over the entire catchment are illustrated in Figures 9 and 10 as basic site information for the interpretation of the results given in the following sections. The arrows indicate the positive direction of the net fluxes, i.e. reaching or leaving the earth surface dependent on the sign of their monthly mean absolute values. Of the net radiation, 82% leaves the catchment as latent heat, 14% leaves as sensible heat and 4% enters the soil in the form of soil heat fluxes. In turn, the latter contribution is partially radiated back as longwave emission from the soil and could have brought about a slight increase of mean soil temperature, which, however, we are not able to assess with precision. The water balance is positive only during one-third of the year, mainly from May to July. Around 47% of the precipitation leaves the catchment as discharge and approximately 53% as evapotranspiration, particularly in the months December and January, where snow contributes a significant fraction to total precipitation.

Soil moisture

In Figure 11, the distributed monthly mean relative soil water content is given. The soil water patterns are mainly influenced by terrain properties as some depressions are fully saturated throughout the year and the slopes in the southern part of the catchment show the lowest saturation (compare Figures 1 and 2b). Further, clear patterns are shaped by the *Histosol* and the water body because of the

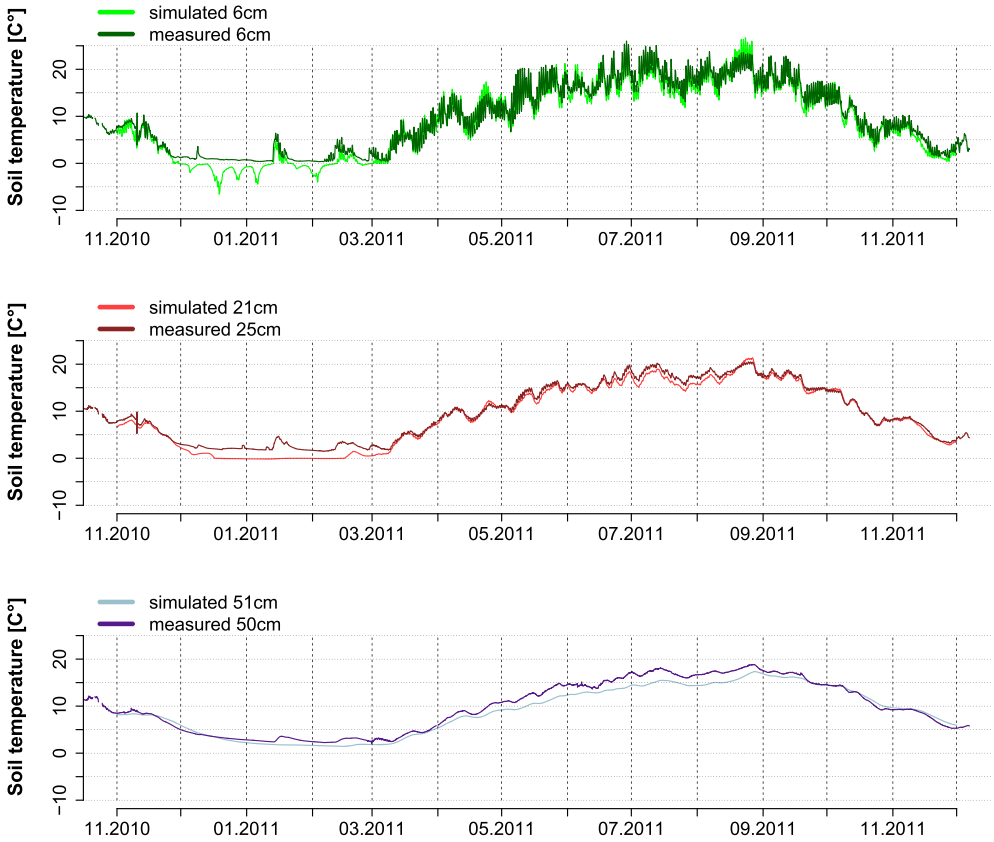

Figure 8. Simulated soil temperatures for different depths compared with measurements from the Terrestrial Environmental Observatories pre-alpine observatory Fendt for the validation period. The R^2s for the different soil layers from top to bottom are 0.93, 0.99 and 0.70

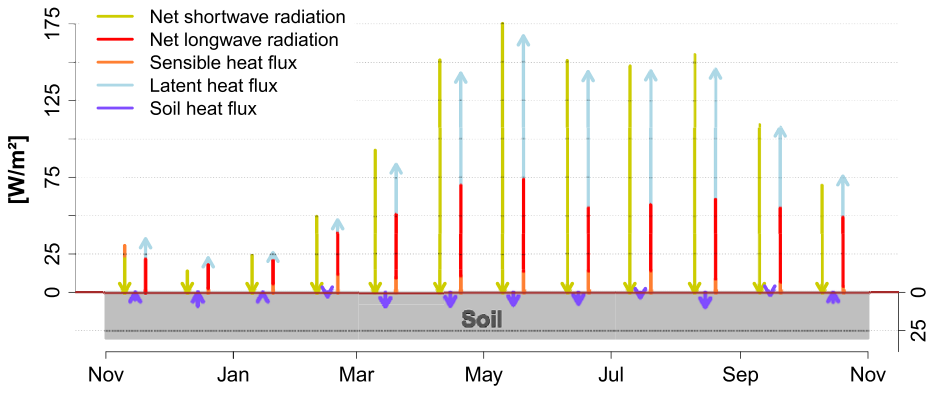

Figure 9. Energy balance of the Rott catchment showing absolute monthly means of simulated energy fluxes and the longwave and shortwave net radiation as areal averages of the whole basin for the hydrological year 2011

selected parameterization. The annual cycle of soil moisture is clearly governed by temperature in winter and precipitation amount in the rest of the year. In January, almost the entire catchment is saturated as a result of soil freezing and a low evapotranspiration (Figure 11). Through thawing in March, the soil water is mobilized, and an increasing radiation input enhances evapotranspiration, leading together with very little precipitation to relatively dry conditions in the catchment. From May to July, the soil water content increases because of an increasing precipitation input (Figure 5). Decreasing precipitation results in dryer conditions in September.

Latent heat flux

With respect to the latent heat fluxes in Figure 12, the highest values occur in May for the land use types *coniferous* and *mixed forest*. These clearly defined spatial

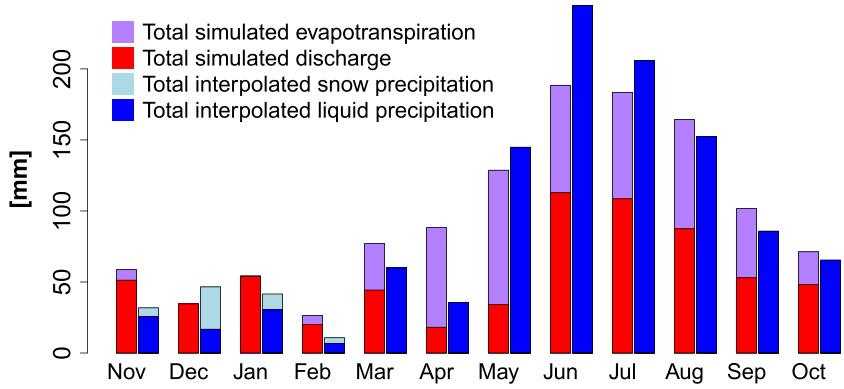

Figure 10. Water balance of the Rott catchment showing the sum of the simulated monthly evapotranspiration and liquid water leaving the catchment as discharge at the gauge Raisting compared with interpolated monthly snow and liquid precipitation sums over the whole basin for the hydrologic year 2011

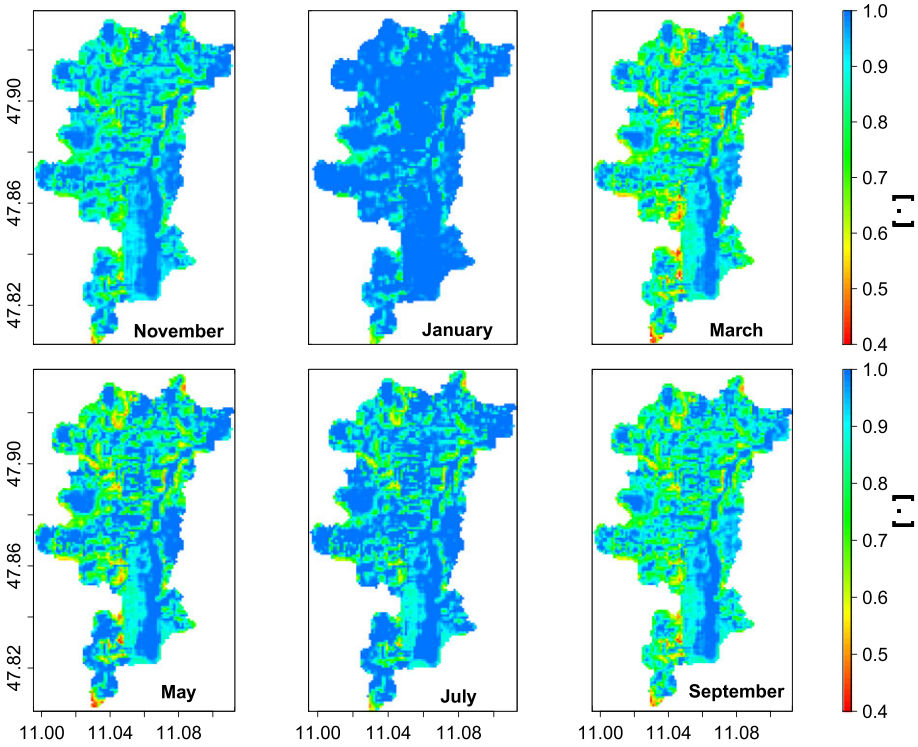

Figure 11. Distributed monthly mean relative soil water content of the uppermost 31 cm of the soil for the hydrological year 2011. The influence of the terrain and the soil type *Histosol* on soil moisture becomes clearly visible (compare Figures 1 and 2a)

patterns become indistinct in January, when the latent heat fluxes reach their minima. These temporal dynamics are controlled by the annual cycle of the radiative forcing (Figure 9) and by the water availability at the surface and in the soil (Figure 11). The lowest values of latent heat flux in the study area are simulated for the land use type *settlement*.

This is due to the parameter vegetation cover fraction being responsible for the split between evaporation, transpiration and interception (Equations A7, A8, A9) and to the parameters canopy density and canopy height, which control the intensity of turbulent energy transport. The values for vegetation cover fraction used in the model are 1.0 for *forest*, 0.9 for *pasture* and 0.1 for *settlement*. Transpiration and evaporation from interception storage correspondingly contribute more to the latent heat flux than soil evaporation. In the southern part of the study area, the shape of the soil type *Histosol* in Figure 12 dominates with slightly higher values than the surrounding area throughout the year. The soil resistance of this soil type is relatively low because of its high actual soil water content.

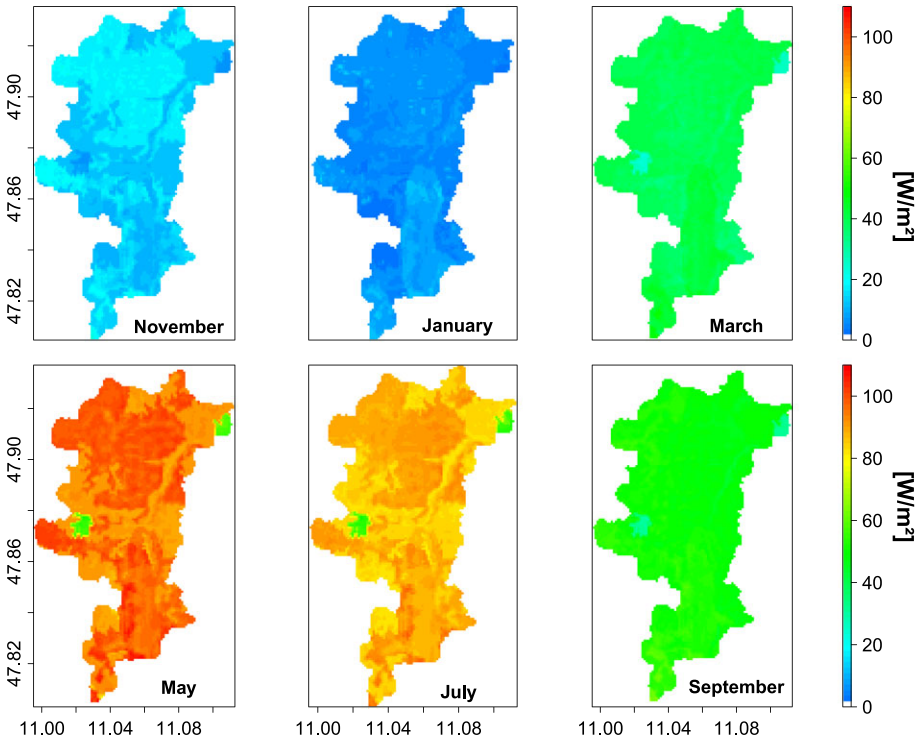

Figure 12. Distributed monthly mean latent heat fluxes for the hydrological year 2011

Sensible heat flux

In case of the spatial distribution of sensible heat fluxes, similar spatial patterns can be observed (Figure 13). However, their spatial maxima and minima show an antipodal behaviour compared with latent heat fluxes (Figure 12), with the highest values for the land use type *settlement* and the lowest over *coniferous forest*. This is due to the high latent heat flux over *forest* and the constraints of total fluxes by the energy balance closure. For the calculation of sensible heat flux from vegetation, soil temperature in Equation 5 is replaced by vegetation temperature. With increasing vegetation cover fraction, the portion of roots in every soil layer f^i_{root} in the numerator of Equation A9 and the low resistance parameters of vegetation r^i_c in the denominator lead to an energy partitioning in favour of latent heat.

Particularly in summer, a gradient in sensible heat flux appears towards higher elevations in the western and southern parts of the catchment (Figures 1 and 13). With increasing altitude, the sensible heat flux also increases as a result of a higher temperature gradient between the surface and the atmosphere due to the altitude-dependent interpolation of air temperature in the model. The blue spots in the southernmost part of the catchment, which appear between September and March, indicate sensible heat fluxes towards the surface. A low volumetric water content of the soil (Figure 11) in this particular area results in a low heat capacity. Thus, the low heat storage of the soil and the vegetation height of *coniferous forest*, which inhibits turbulent energy exchange with the atmosphere (taken into account by the zero-plane displacement height), keep the daily temperature amplitudes lower than those in the overlying atmosphere, thereby causing heat fluxes towards the surface. In January, the high water content and thus the high heat capacity of the soil type *Histosol* have a similar effect on the heat gradient between soil and atmosphere as the forest is shaping an area of relatively low fluxes.

With respect to the annual cycle, the maxima and minima are shifted compared with the latent heat flux. In November, the fluxes turn towards the surface nearly over the entire catchment, because of the atmosphere being warmer than the soil (Figures 8 and 9). This gradient is shifted again in January, because of a very low air temperature and a negative soil heat flux (Figure 14). The maximum sensible heat flux is reached in July, when the soil is warm from intense heating in May and June and the atmosphere has already cooled because of the decreasing incident radiation (Figure 9).

Soil heat flux

Compared with the turbulent fluxes, the soil heat flux shows less spatial variability but with still noticeable influence of land use and soil type (Figure 14). Particularly, the *Histosol* shows a smoothing effect on the amplitude of the annual evolution of the soil heat flux,

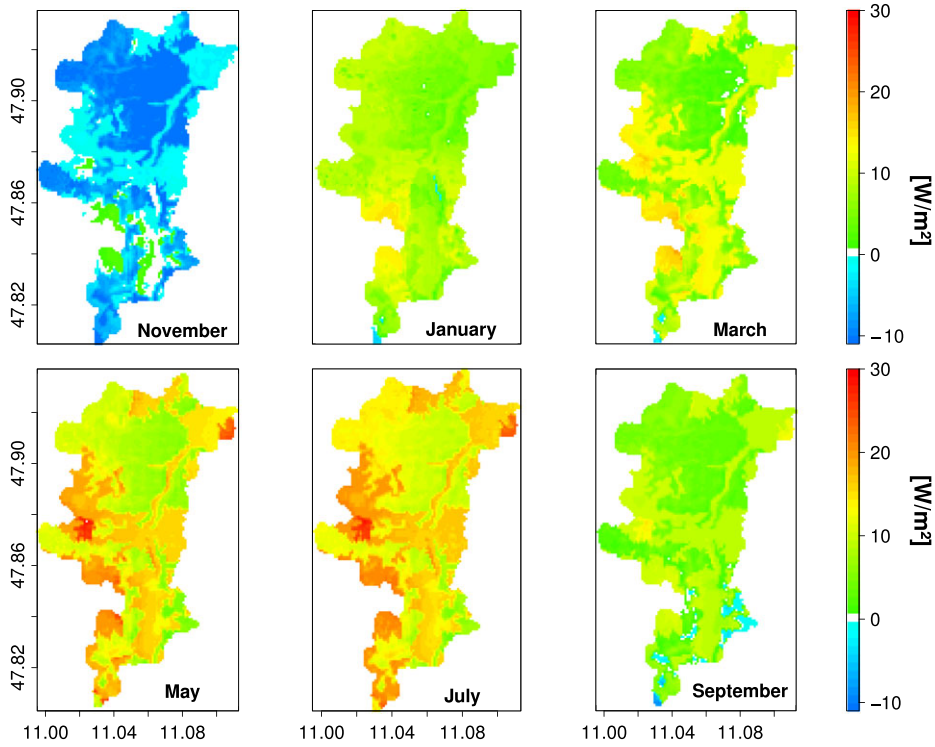

Figure 13. Distributed monthly mean sensible heat fluxes for the hydrological year 2011

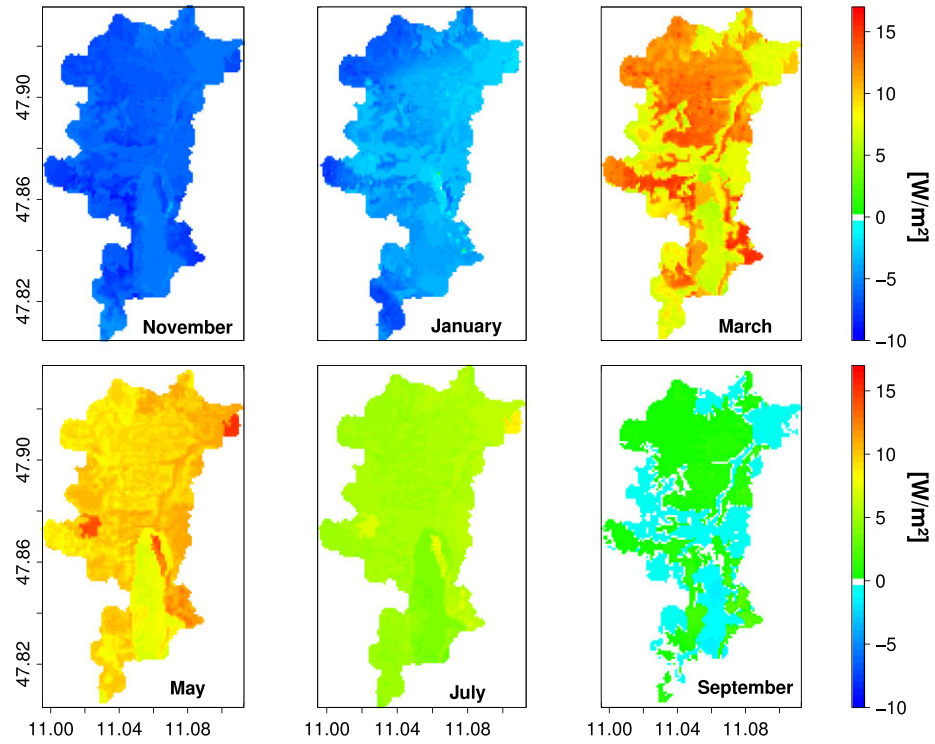

Figure 14. Distributed monthly mean soil heat fluxes for the hydrological year 2011

owing to its high water content (Figure 11) and the low heat conductivity of its solid phase. Unlike that in the turbulent fluxes, the temporal occurrence of maxima and minima differs between the land use types. The spatial patterns of areas classified as *coniferous* and *mixed forest* in Figure 2 appear clearly with maximum soil heat fluxes

in March. Responsible for these differences is mainly the average vegetation height, which controls the wind profile within the canopy and thus the turbulent exchange. In March, the turbulent fluxes (Figures 12 and 13) are quite low over the forested areas, but relatively high for the land use type *settlement* with little vegetation and energy transport from the surface to the atmosphere. Within the canopy of the forest, turbulent exchange is inhibited through the high vegetation; hence, the available energy from increasing radiation input in spring (Figure 9) is absorbed by the cold soil. In May, heat gradients between the surface and the atmosphere become lower in the forest, because of the preceding warming of the soil and the absorption of solar radiation by vegetation cover. The 90% bare soil fraction for the land use type *settlement*, in contrast, absorbs large amounts of the incoming solar radiation, leading to high soil heat fluxes and sensible heat fluxes (Figures 13 and 14). This effect of inhibiting turbulent exchange by high vegetation can also be observed in September, when mean soil heat fluxes in forests are still positive, while they turned negative because of a reversed heat gradient for the other land use types. For all three flux types, areas of uniform fluxes (appearing particularly during periods of intensive energy exchange) show patterns, similar to the maps of land use and soil type in Figure 2. However, the impact of different vegetation classifications is more dominant than that of soil types, highlighting the dominant role of vegetation in energy partitioning. Maxima and minima differ between fluxes as well as in space and time.

PARTITIONING OF WATER AND ENERGY FLUXES FOR SELECTED LAND USE TYPES

In Figure 15, the monthly energy balances for the land use types *coniferous forest*, *pasture* and *settlement* are illustrated for the validation period. These land use types are selected because they differ in their characteristics like vegetation height and density. All fluxes of one land use type have been averaged over an area in the range of 500- to 700-m altitude and only at the soil type *Lessive*, because only this soil type is covered with all of the described land use types and a great part of the catchment is within this altitudinal range. In doing so, the effects of topography and different soils on the fluxes are minimized to emphasize their intrinsic disparities and to improve comparability. In each panel of Figure 15, the top plot shows fluxes above vegetation, i.e. net radiative and turbulent fluxes; the middle panels the energy amount absorbed and emitted by the vegetation canopy; and the bottom panels the energy amount absorbed and emitted by the soil, including the soil heat flux. All three land use types show similar dynamics of ingoing and outgoing fluxes above the canopy following the seasonal cycle of radiative forcing. A major difference is the partitioning of the incoming shortwave radiation into longwave radiation and turbulent fluxes. With increasing vegetation density and height from *settlement* to *forest*, the evapotranspiration, i.e., the latent heat flux, increases and the sensible heat flux and the longwave radiation decrease. This is due to physiological properties of plants, which have very efficient mechanisms to dissipate heat by transpiration. The roots allow plants to absorb water from deep soil layers, and leaves provide a big area for transpiration (Hammerle *et al*., 2008; Brümmer *et al*., 2012). The higher the vegetation, the more soil volume is perforated by roots, and higher leaf areas enhance not only transpiration but also evaporation of intercepted water (Ringgaard *et al*., 2011). For *settlements* with no or very scarce vegetation cover compared with *pasture* and *forest*, a bigger part of the energy leaves the earth surface in the form of longwave radiation and sensible heat flux as a result of high surface temperatures of bare soil. A negligible part of the energy is converted by the vegetation cover. Hence, the latent heat flux over *settlement* is determined by evaporation. This is in contrast to *pasture* and *forest*, where latent heat originates mainly from plant transpiration and makes a major contribution to the energy fluxes, illustrating the dominant role of plant transpiration on energy partitioning (Bultot *et al*., 1990; Ringgaard *et al*., 2011). Incoming and outgoing energy fluxes are not necessarily equal, because a portion of the energy is stored in either the soil or the vegetation or the atmosphere below and above the canopy. This change in heat storage is evident in the soil heat flux in the bottom panels of the plots. From September to January, when more energy is emitted from the surface than is absorbed, the soil heat flux turns upwards, transporting heat from the soil storage to the surface. During the summer months, the heat storage change in the soil is positive with soil heat fluxes from the surface into the soil. The biggest soil heat fluxes occur for *settlements*, with low vegetation cover and therefore high surface temperature changes. At densely vegetated surfaces like *forests* in Figure 15a, the buffering function of vegetated surfaces becomes evident. In November, for instance, a considerably larger amount of energy is absorbed by vegetation than emitted. During the summer months, heat stored in the vegetation and the air below the canopy are emitted into the atmosphere above and absorbed by the soil simultaneously. But the sum of incoming and outgoing energy and the soil heat flux for each month does not equal zero in contrast to the fluxes at the land use type *settlement* in Figure 15c. This means that there has to be a kind of storage function of vegetated surfaces. In the model, heat can be stored in water, in the air and in the solid part of the soil because of their respective heat capacity, which however would not be enough for this amount of energy. In the literature (e.g. Bonan, 2008), this energy is contributed

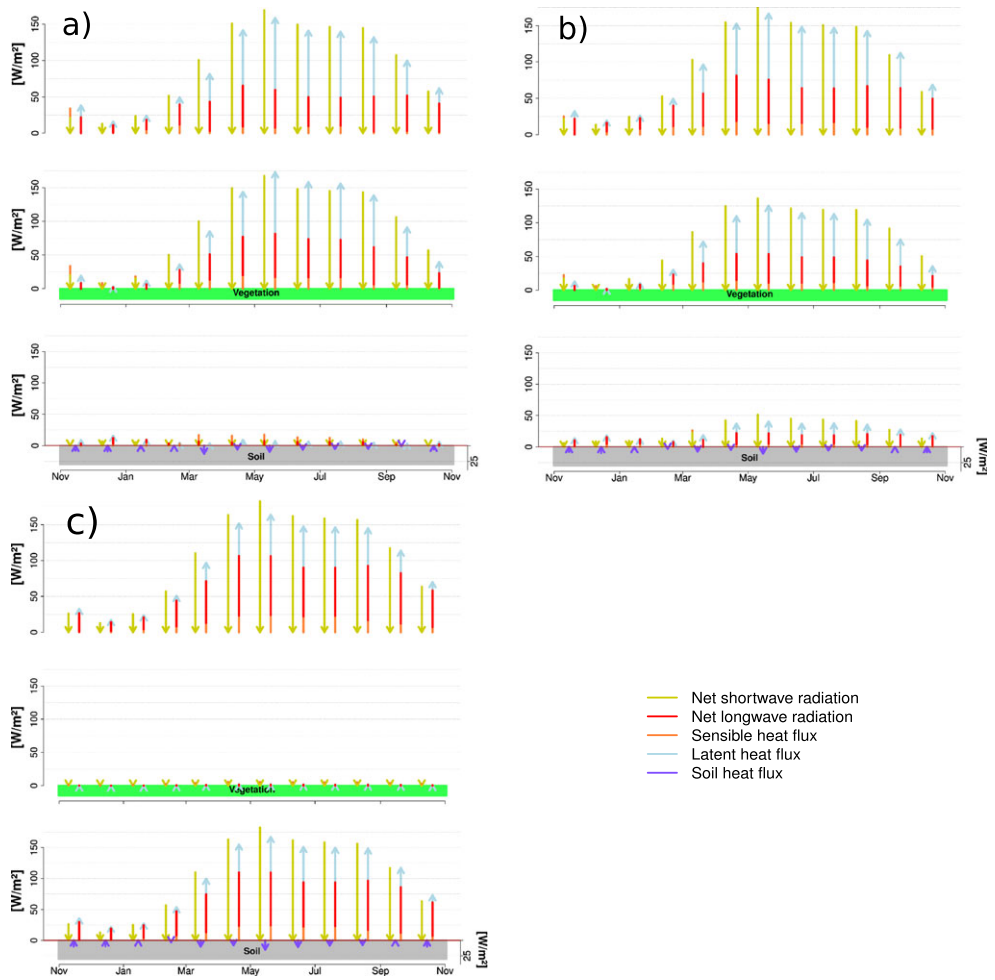

Figure 15. Energy balance for the land use types *coniferous forest* (a), *pasture* (b) and *settlement* (c) showing absolute monthly means of simulated energy fluxes and the longwave and shortwave net radiation for the hydrological year 2011. The upper panels of each plot show incoming and outgoing radiation and fluxes above the canopy, the middle panels the absorbed and emitted energy amount by the canopy and the bottom panels the energy balance at the soil surface

to plant assimilation, i.e. it is transferred to biomass. This process however is not included in our model, but the energy balance is preserved. Hence, we interpret this behaviour as energy pending within the canopy between the plants, the canopy air and the soil because dense vegetation inhibits the exchange of energy with the overlying atmosphere. This energy exchange between canopy, canopy air and soil highlights the buffering effect of vegetated surfaces on atmospheric influences.

SUMMARY AND CONCLUSIONS

This study has set a focus on the joint analysis of both water and energy fluxes in a small mesoscale catchment (55 km^2) in Southern Germany. We analysed distributed modelling results and micrometeorological measurements in addition to traditional streamflow observations at the outlet of the catchment. We showed the technical and conceptual feasibility of a joint and closed water and energy balance analysis for the hydrological years 2010–2011 and for the specific scale of this catchment. The peculiar value of this approach is the possibility to analyse single processes of the water and energy balance, taking into account mutual interdependencies. The scientific implication lies in the detailed derivation of the mutual interdependencies of spatio-temporal water and energy flux variability.

We used a physically based model with a three-dimensional treatment of water dynamics in the saturated and unsaturated zone solving the Richards equation as well as the energy balance components linked to soil moisture states. The simulation results were validated against hourly discharge and energy flux measurements taken from an EC station. In addition, the plausibility of their spatial patterns and partitioning at different land use types was analysed.

Reasonable results were obtained for the discharge with reasonable congruency between simulated and measured hydrographs at the outlet of the catchment for both the

calibration year 2010 and the validation year 2011, however with an overestimation of discharge volumes. Although no calibration of the sensible parameters to the energy balance components was performed, a moderate to good model performance was achieved for the simulation of hourly energy fluxes and further variables measured at the EC station. Water and energy balance components and partitioning at different land use types were analysed. The spatial distribution of the energy balance components shows reasonable patterns with clear differences between the land use and soil types derivable of their respective parameterization. The analysis of energy partitioning for different land use types reveals good congruency with the prevailing surface and subsurface processes. A working point and limitation of the model is an overestimation of the latent heat flux and an underestimation of the sensible heat flux, soil heat flux and soil temperature. This might be due to deficiencies in the parameterization of the soil or the vegetation, but it may also shed light on the possible sinks of the lost energy in the energy balance closure problem prevalent in EC measurements.

In future studies, the additional consideration of energy fluxes in hydrological models may allow an improved estimation of model parameters as they put further constraints on the parameter sets and reduce the ambiguity of the solution. Only when hydrological variables beyond discharge measurements are considered, a further in-depth understanding of hydrological processes be achieved. This will be facilitated by an increasing number of hydrometeorological test beds that provide compartment crossing observations, in particular energy flux measurements.

ACKNOWLEDGEMENTS

Special thanks go to the German Weather Service (*DWD*), the Bavarian flood forecasting service *HND* and the Wasserwirtschaftsamt Weilheim for providing meteorological and discharge observations. TERENO infrastructure (www.tereno.net), funded by Helmholtz Association, is gratefully acknowledged. Thanks also to Dr Michael Warscher (KIT) for proofreading. Comments from two anonymous reviewers helped to improve the manuscript significantly and are highly appreciated.

REFERENCES

Abbott MB, Bathurst JC, Cunge JA, O'Connell PE, Rasmussen J. 1986. An introduction to the European Hydrological System – Systeme Hydrologique Europeen, SHE, 1: History and philosophy of a physically-based, distributed modelling system. *Journal of Hydrology* **87**(1): 45–59.

Abera W, Antonello A, Franceschi S, Formetta G, Rigon R. 2014. The Udig Spatial Toolbox for hydro-geomorphic analysis geomorphological techniques. British Society for Geomorphology.

Abramowitz G, Leuning R, Clark M, Pitman A. 2008. Evaluating the performance of land surface models. *Journal of Climate* **21**(21): 5468–5481.

Arnault J, Wagner S, Rummler T, Fersch B, Bliefernicht J, Andresen S, Kunstmann H. 2015. Role of runoff-infiltration partitioning and resolved overland flow on land-atmosphere feedbacks: a case-study with the WRF-Hydro coupled modeling system for West Africa. *Journal of Hydrometeorology*. DOI:10.1175/JHM-D-15-0089.1

Arnold JG, Srinivasan R, Muttiah RS, Williams JR. 1998. Large area hydrologic modeling and assessment part I: model development. *JAWRA Journal of the American Water Resources Association* **34**(1): 73–89.

Bahrenberg G, Giese E, Nipper J. 1992. *Multivariate Statistik*, **2**. Teubner: Leipzig, Germany.

Baldocchi D et al. 2001. Fluxnet: a new tool to study the temporal and spatial variability of ecosystem-scale carbon dioxide, water vapor, and energy flux densities. *Bulletin of the American Meteorological Society* **82**(11): 2415–2434.

Band LE. 1993. Effect of land surface representation on forest water and carbon budgets. *Journal of Hydrology* **150**(2): 749–772.

Bertoldi G, Della Chiesa S, Notarnicola C, Pasolli L, Niedrist G, Tappeiner U. 2014. Estimation of soil moisture patterns in mountain grasslands by means of SAR RADARSAT2 images and hydrological modeling. *Journal of Hydrology* **516**: 245–257.

Bertoldi G, Notarnicola C, Leitinger G, Endrizzi S, Zebisch M, Della Chiesa S, Tappeiner U. 2010. Topographical and ecohydrological controls on land surface temperature in an alpine catchment. *Ecohydrology* **3**(2): 189–204.

Bertoldi G, Rigon R, Over T. 2006. Impact of watershed geomorphic characteristics on the energy and water budgets. *Journal of Hydrometeorology* **7**(3): 389–403.

Bertoldi G, Tamanini D, Zanotti F, Rigon R. 2004. *GEOTOP: A Hydrological Balance Model. Technical Description and Programs Guide*. University of Trento: Italy.

Best M et l. 2011. The Joint UK Land Environment Simulator (JULES), model description – part 1: energy and water fluxes. *Geoscientific Model Development* **4**(3): 677–699.

Betts AK, Ball JH, Beljaars A, Miller MJ, Viterbo PA. 1996. The land surface–atmosphere interaction: a review based on observational and global modeling perspectives. *Journal of Geophysical Research, [Atmospheres]* **101**(D3): 7209–7225.

Betts AK, Desjardins R, Worth D, Cerkowniak D. 2013. Impact of land use change on the diurnal cycle climate of the Canadian Prairies. *Journal of Geophysical Research [Atmospheres]* **118**(21): 1996–12011. DOI:10.1002/2013JD020717

Bixio AC, Orlandini S, Paniconi C, Putti M. 2000. Physically-based distributed model for coupled surface runoff and subsurface flow simulation at the catchment scale. In *Computational Methods in Water Resources*, **2**; 1115–1122.

Bliefernicht J et al. 2013. Field and simulation experiments for investigating regional land–atmosphere interactions in West Africa: Experimental set-up and first results. *IAHS-AISH Publication* **359**: 226–232.

Bonan GB. 2008. Forests and climate change: forcings, feedbacks, and the climate benefits of forests. *Science* **320**(5882): 1444–1449.

Brümmer C et al. 2012. How climate and vegetation type influence evapotranspiration and water use efficiency in Canadian forest, peatland and grassland ecosystems. *Agricultural and Forest Meteorology* **153**: 14–30.

Brutsaert W. 1975. On a derivable formula for long-wave radiation from clear skies. *Water Resources Research* **11**(5): 742–744.

Brutsaert W. 1982. *Evaporation into the Atmosphere: Theory, History, and Applications*, **1**. Springer.

Bultot F, Dupriez G, Gellens D. 1990. Simulation of land use changes and impacts on the water balance: a case study for Belgium. *Journal of Hydrology* **114**(3): 327–348.

Chahine M, Vane D. 1995. GEWEX: the global energy and water cycle experiment. *Eos, Transactions American Geophysical Union* **73**: 9–14.

Chen F, Dudhia J. 2001. Coupling an advanced land surface-hydrology model with the Penn State-NCAR MM5 modeling system. Part I: model implementation and sensitivity. *Monthly Weather Review* **129**(4): 569–585.

Chen JM, Chen X, Ju W, Geng X. 2005. Distributed hydrological model for mapping evapotranspiration using remote sensing inputs. *Journal of Hydrology* **305**(1): 15–39.

Ciarapica L, Todini E. 2002. TOPKAPI: a model for the representation of the rainfall–runoff process at different scales. *Hydrological Processes* **16**(2): 207–229.

Clark D et al. 2011. The Joint UK Land Environment Simulator (JULES), model description – part 2: carbon fluxes and vegetation dynamics. *Geoscientific Model Development* **4**(3): 701–722.

Cuo L, Lettenmaier DP, Mattheussen BV, Storck P, Wiley M. 2008. Hydrologic prediction for urban watersheds with the distributed hydrology–soil–vegetation model. *Hydrological Processes* **22**(21): 4205–4213.

Dai Y et al. 2003. The common land model. *Bulletin of the American Meteorological Society* **84**(8): 1013–1023.

Dall' Amico M, Endrizzi S, Gruber S, Rigon R. 2011. A robust and energy-conserving model of freezing variably-saturated soil. *The Cryosphere* **5**(2): 469–484.

De Roo A, Wesseling C, Van Deursen W. 2000. Physically based river basin modelling within a GIS: the LISFLOOD model. *Hydrological Processes* **14**(11-12): 1981–1992.

Decker M, Brunke MA, Wang Z, Sakaguchi K, Zeng X, Bosilovich MG. 2012. Evaluation of the reanalysis products from GSFC, NCEP, and ECMWF using flux tower observations. *Journal of Climate* **25**(6): 1916–1944.

Della Chiesa S et al. 2014. Modelling changes in grassland hydrological cycling along an elevational gradient in the Alps. *Ecohydrology* **7**(6): 1453–1473.

Dirmeyer PA, Niyogi D, de Noblet-Ducoudré N, Dickinson RE, Snyder PK. 2010. Impacts of land use change on climate. *International Journal of Climatology* **30**(13): 1905–1907.

Drewry D, Kumar P, Long S, Bernacchi C, Liang X-Z, Sivapalan M. 2010. Ecohydrological responses of dense canopies to environmental variability: 1. Interplay between vertical structure and photosynthetic pathway. *Journal of Geophysical Research, Biogeosciences* **115**(G4).

Eder F, De Roo F, Kohnert K, Desjardins RL, Schmid HP, Mauder M. 2014. Evaluation of two energy balance closure parametrizations. *Boundary-Layer Meteorology* **151**(2): 195–219.

Endrizzi S, Gruber S, Dall'Amico M, Rigon R. 2014. GEOtop 2.0: simulating the combined energy and water balance at and below the land surface accounting for soil freezing, snow cover and terrain effects. *Geoscientific Model Development* **7**(6): 2831–2857.

Endrizzi S, Marsh P. 2010. Observations and modeling of turbulent fluxes during melt at the shrub–tundra transition zone 1: point scale variations. *Hydrology Research* **41**(6): 471–491.

Famiglietti J, Wood E. 1994. Multiscale modeling of spatially variable water and energy balance processes. *Water Resources Research* **30**(11): 3061–3078.

FAO, ISRIC, *et al*. 1998. World reference base for soil resources. *World Soil Resources Reports* **84**: 21–22.

Fatichi S, Ivanov VY, Caporali E. 2012. A mechanistic ecohydrological model to investigate complex interactions in cold and warm water-controlled environments: 1. Theoretical framework and plot-scale analysis. *Journal of Advances in Modeling Earth Systems* **4**: M05002. DOI:10.1029/2011MS000086

Foken T, Göckede M, Mauder M, Mahrt L, Amiro B, Munger W. 2005. Post-field data quality control. In *Handbook of Micrometeorology*; 181–208.

Foken T et al. 2010. Energy balance closure for the LITFASS-2003 experiment. *Theoretical and Applied Climatology* **101**(1–2): 149–160.

Foley JA, Levis S, Costa MH, Cramer W, Pollard D. 2000. Incorporating dynamic vegetation cover within global climate models. *Ecological Applications* **10**(6): 1620–1632.

Formetta G, Rigon R, Chávez J, David O. 2013. Modeling shortwave solar radiation using the JGrass-NewAge system. *Geoscientific Model Development* **6**(4): 915–928.

Gao, H., et al., 2010: Water budget record from variable infiltration capacity (VIC) model. *Algorithm Theoretical Basis Document for Terrestrial Water Cycle Data Records*.

Gebremichael M, Rigon R, Bertoldi G, Over T. 2009. On the scaling characteristics of observed and simulated spatial soil moisture fields. *Nonlinear Processes in Geophysics* **16**(1): 141–150.

Gochis, D., W. Yu, and D. Yates, 2013: The WRF-Hydro model technical description and user's guide, version 1.0. *NCAR Technical Document*, **120**.

Graham, D. N. and M. B. Butts, 2005: Flexible, integrated watershed modelling with MIKE SHE. *Watershed Models*, 245–272.

Grant, G., M. Firestone, and L. Derry, 2012: Critical zone observatory steering committee report June, 25 2012. Tech. rep.

Gubler S, Endrizzi S, Gruber S, Purves R. 2013. Sensitivities and uncertainties of modeled ground temperatures in mountain environments. *Geoscientific Model Development* **6**(4): 1319–1336.

Hammerle, A., A. Haslwanter, U. Tappeiner, A. Cernusca, and G. Wohlfahrt, 2008: Leaf area controls on energy partitioning of a temperate mountain grassland. *Biogeosciences* (*online*), **5**(2).

Hogue TS, Bastidas L, Gupta H, Sorooshian S, Mitchell K, Emmerich W. 2005. Evaluation and transferability of the Noah land surface model in semiarid environments. *Journal of Hydrometeorology* **6**(1): 68–84.

Ivanov VY, Bras RL, Vivoni ER. 2008a. Vegetation–hydrology dynamics in complex terrain of semiarid areas: 1. A mechanistic approach to modeling dynamic feedbacks. *Water Resources Research* **44**(3).

Ivanov VY, Bras RL, Vivoni ER. 2008b. Vegetation–hydrology dynamics in complex terrain of semiarid areas: 2. Energy-water controls of vegetation spatiotemporal dynamics and topographic niches of favorability. *Water Resources Research* **44**(3): W03430. DOI:10.1029/2006WR005595

Ivanov VY, Vivoni ER, Bras RL, Entekhabi D. 2004. Catchment hydrologic response with a fully distributed triangulated irregular network model. *Water Resources Research* **40**(11): W11102. DOI:10.1029/2004WR003218

Kitanidis PK. 1997. *Introduction to Geostatistics: Applications to Hydrogeology*. Cambridge University Press: Cambridge, UK; 252.

Kollet SJ, Maxwell RM. 2008. Capturing the influence of groundwater dynamics on land surface processes using an integrated, distributed watershed model. *Water Resources Research* **44**(2): 665–669.

Krysanova V, Arnold JG. 2008. Advances in ecohydrological modelling with SWAT – a review. *Hydrological Sciences Journal* **53**(5): 939–947.

Kunstmann H, Krause J, Mayr S. 2006. Inverse distributed hydrological modelling of Alpine catchments. *Hydrology and Earth System Sciences* **10**(3): 395–412.

Kunstmann H, Schneider K, Forkel R, Knoche R. 2004. Impact analysis of climate change for an Alpine catchment using high resolution dynamic downscaling of ECHAM4 time slices. *Hydrology and Earth System Sciences* **8**(6): 1031–1045.

Larsen MAD, Refsgaard JC, Drews M, Butts MB, Jensen KH, Christensen J, Christensen O. 2014. Results from a full coupling of the HIRHAM regional climate model and the MIKE SHE hydrological model for a Danish catchment. *Hydrology and Earth System Sciences* **18**(11): 4733–4749.

Lawford RG, Roads J, Lettenmaier DP, Arkin P. 2007. GEWEX contributions to large-scale hydrometeorology. *Journal of Hydrometeorology* **8**(4): 629–641.

Lawrence DM et al. 2011. Parameterization improvements and functional and structural advances in version 4 of the Community Land Model. *Journal of Advances in Modeling Earth Systems* **3**(1).

Liang, X., D. P. Lettenmaier, E. F. Wood, and S. J. Burges, 1994. A simple hydrologically based model of land surface water and energy fluxes for general circulation models. *Journal of Geophysical Research: Atmospheres* (*1984–2012*), **99**(D7), 14415–14428.

Lindroth A, Mölder M, Lagergren F. 2010. Heat storage in forest biomass improves energy balance closure. *Biogeosciences* **7**(1): 301–313.

Mauder M, Cuntz M, Drüe C, Graf A, Rebmann C, Schmid HP, Schmidt M, Steinbrecher R. 2013. A strategy for quality and uncertainty assessment of long-term eddy-covariance measurements. *Agricultural and Forest Meteorology* **169**: 122–135.

Mauder, M. and T. Foken, 2015: Eddy-covariance software TK3. DOI:10.5281/zenodo.20349.

Mauder M, Liebethal C, Göckede M, Leps JP, Beyrich F, Foken T. 2006. Processing and quality control of flux data during LITFASS-2003. *Boundary-Layer Meteorology* **121**(1): 67–88.

Maxwell RM, Kollet SJ. 2008. Interdependence of groundwater dynamics and land-energy feedbacks under climate change. *Nature Geoscience* **1**(10): 665–669.

Montaldo N, Rondena R, Albertson JD, Mancini M. 2005. Parsimonious modeling of vegetation dynamics for ecohydrologic studies of water-limited ecosystems. *Water Resources Research* **41**(10).

Nash JE, Sutcliffe JV. 1970. River flow forecasting through conceptual models part IA discussion of principles. *Journal of Hydrology* **10**(3): 282–290.

Newman BD et al. 2006. Ecohydrology of water-limited environments: a scientific vision. *Water Resources Research* **42**(6).
Niu G-Y, Paniconi C, Troch PA, Scott RL, Durcik M, Zeng X, Huxman T, Goodrich DC. 2014. An integrated modelling framework of catchment-scale ecohydrological processes: 1. Model description and tests over an energy-limited watershed. *Ecohydrology* **7**(2): 427–439.
Niu G-Y et al. 2011. The community Noah land surface model with multiparameterization options (Noah-MP): 1. Model description and evaluation with local-scale measurements. *Journal of Geophysical Research [Atmospheres]* **116**(D12).
Ott I et al. 2013. High-resolution climate change impact analysis on medium-sized river catchments in Germany: an ensemble assessment. *Journal of Hydrometeorology* **14**(4): 1175–1193.
Overgaard J, Rosbjerg D, Butts M. 2005. Land-surface modelling in hydrological perspective. *Biogeosciences Discussions* **2**(6): 1815–1848.
Paniconi C, Putti M. 1994. A comparison of Picard and Newton iteration in the numerical solution of multidimensional variably saturated flow problems. *Water Resources Research* **30**(12): 3357–3374.
Pielke RA, Avissar R, Raupach M, Dolman AJ, Zeng X, Denning AS, et al. 1998. Interactions between the atmosphere and terrestrial ecosystems: influence on weather and climate. *Global Change Biology* **4**(5): 461–475.
Pielke RA et al. 2011. Land use/land cover changes and climate: modeling analysis and observational evidence. *Wiley Interdisciplinary Reviews: Climate Change* **2**(6): 828–850.
Pitman A. 2003. The evolution of, and revolution in, land surface schemes designed for climate models. *International Journal of Climatology* **23**(5): 479–510.
Prentice IC, Liang X, Medlyn B, Wang Y-P. 2015. Reliable, robust and realistic: the three r's of next-generation land-surface modelling. *Atmospheric Chemistry and Physics* **15**(10): 5987–6005.
Refshaard J, Storm B, Singh V, et al. 1995. MIKE SHE. In *Computer Models of Watershed Hydrology*; 809–846.
Rigon R, Bertoldi G, Over TM. 2006. GEOtop: a distributed hydrological model with coupled water and energy budgets. *Journal of Hydrometeorology* **7**(3): 371–388.
Ringgaard R, Herbst M, Friborg T, Schelde K, Thomsen AG, Soegaard H. 2011. Energy fluxes above three disparate surfaces in a temperate mesoscale coastal catchment. *Vadose Zone Journal* **10**(1): 54.
Rodriguez-Iturbe I. 2000. Ecohydrology: a hydrologic perspective of climate–soil–vegetation dynamics. *Water Resources Research* **36**(1): 3–9.
Rodriguez-Iturbe I, Rinaldo A. 1997. *Fractal River Networks: Chance and Self-organization*. Cambridge University Press: New York, USA.
Rosero, E., Z.-L. Yang, T. Wagener, L. E. Gulden, S. Yatheendradas, and G.-Y. Niu, 2010: Quantifying parameter sensitivity, interaction, and transferability in hydrologically enhanced versions of the Noah land surface model over transition zones during the warm season. *Journal of Geophysical Research: Atmospheres* (*1984–2012*), **115**(D3).
Roy SS, Mahmood R, Niyogi D, Lei M, Foster SA, Hubbard KG, Douglas E, Pielke RA Sr. 2007. Impacts of the agricultural Green Revolution-induced land use changes on air temperatures in India. *Journal of Geophysical Research* **112**(D21).
Schulla, J. and K. Jasper, 2015: Model description WaSiM. *Technical Report*, pp. 332, Zürich.
Seneviratne SI, Corti T, Davin EL, Hirschi M, Jaeger EB, Lehner I, Orlowsky B, Teuling AJ. 2010. Investigating soil moisture–climate interactions in a changing climate: a review. *Earth-Science Reviews* **99**(3): 125–161.
Seneviratne SI, Lüthi D, Litschi M, Schär C. 2006. Land–atmosphere coupling and climate change in Europe. *Nature* **443**(7108): 205–209.
Shen C, Niu J, Phanikumar MS. 2013. Evaluating controls on coupled hydrologic and vegetation dynamics in a humid continental climate watershed using a subsurface–land surface processes model. *Water Resources Research* **49**(5): 2552–2572.
Singh VP, Frevert DK. 2010. *Watershed Models*. CRC Press.
Smiatek G, Kunstmann H, Werhahn J. 2012. Implementation of a high performance analysis of a high resolution coupled numerical weather and river runoff prediction model system for a alpine catchment. *Environmental Modeling and Software* **38**: 231–243.
Stoy P et al. 2013. A data-driven analysis of energy balance closure across fluxnet research sites: the role of landscape scale heterogeneity. *Agricultural and Forest Meteorology* **171**: 137–152.
Tague C, Band L. 2004. Rhessys: regional hydro-ecologic simulation system – an object-oriented approach to spatially distributed modeling of carbon, water, and nutrient cycling. *Earth Interactions* **8**(19): 1–42.
Van Der Knijff J, Younis J, De Roo A. 2010. LISFLOOD: a GIS-based distributed model for river basin scale water balance and flood simulation. *International Journal of Geographical Information Science* **24**(2): 189–212.
Vivoni E, Entekhabi D, Bras R, Ivanov V. 2007. Controls on runoff generation and scale-dependence in a distributed hydrologic model. *Hydrology and Earth System Sciences Discussions* **11**(5): 1683–1701.
Vivoni ER, Rodríguez JC, Watts CJ. 2010. On the spatiotemporal variability of soil moisture and evapotranspiration in a mountainous basin within the North American monsoon region. *Water Resources Research* **46**(2).
Wang G, Eltahir EAB. 2000. Modeling the biosphere–atmosphere system: the impact of the subgrid variability in rainfall interception. *Journal of Climate* **13**(16): 2887–2899.
Wigmosta MS, Nijssen B, Storck P, Lettenmaier D. 2002. The distributed hydrology soil vegetation model. In *Mathematical Models of Small Watershed Hydrology and Applications*; 7–42.
Wilson K et al. 2002. Energy balance closure at FLUXNET sites. *Agricultural and Forest Meteorology* **113**(1–4): 223–243.
Yang Z-L et al. 2011. The community Noah land surface model with multiparameterization options (Noah-MP): 2. Evaluation over global river basins. *Journal of Geophysical Research [Atmospheres]* **116**(D12).
Zacharias S et al. 2011. A network of terrestrial environmental observatories in Germany. *Vadose Zone Journal* **10**(3): 955–973.
Zanotti F, Endrizzi S, Bertoldi G, Rigon R. 2004. The GEOTOP snow module. *Hydrological Processes* **18**(18): 3667–3679.
Zhao W, Li A. 2015. A review on land surface processes modelling over complex terrain. *Advances in Meteorology* **2015**: 17, 607181, 17 pages. DOI:10.1155/2015/607181

APPENDIX
THE GEOTOP MODEL: BASIC EQUATIONS AND PARAMETERS

For reasons of completeness, the central process formulations with respect to water and energy fluxes of the GEOtop version 1.45 are summarized.

RADIATION BUDGET

For the net radiation R_n ($W\,m^{-2}$), the following equation is applied (Bertoldi *et al.*, 2004; Rigon *et al.*, 2006; Endrizzi and Marsh, 2010):

$$R_n = [sh(x,t)\cdot R{\downarrow}_{SWP} + V(x)\cdot R{\downarrow}_{SWD}]\cdot[1 - V(x)\cdot a] + V(x)\cdot\varepsilon_a\cdot R{\downarrow}_{LW} - V(x)\cdot\varepsilon_s\cdot\delta\cdot T_s^4 \quad \text{(A1)}$$

Here $R{\downarrow}_{SW}$ ($W\,m^{-2}$) is the shortwave radiation on the surface with the subscript P describing the direct and D the diffuse parts, respectively. The shortwave albedo a (—) includes the reflection of neighbouring slopes with the sky view factor $V(x)$ in $(1 - V(x)\cdot a)$. ε_a (—) is the atmospheric and ε_s (—) the longwave soil or snow emissivity and $R{\downarrow}_{LW}$ ($W\,m^{-2}$) the incoming longwave radiation after Brutsaert (1975). T_s (K) is the surface temperature and δ the Stefan Boltzmann constant $5.6704\cdot10^{-8}$ [$W(m^{-2}\,K^{-4})$].

ENERGY BALANCE

For the calculation of the energy balance, measurements of the air temperature, the wind speed, the relative air moisture, the precipitation amount and the shortwave radiation are used. The energy balance is calculated for every grid box together with the soil water balance as a sum of the energy in the water and in the soil in continuous form as (Rigon *et al.*, 2006; Dall' Amico *et al.*, 2011; 558 Endrizzi *et al.*, 2014)

$$\frac{\partial U(\mathbf{x},t)}{\partial t} + \nabla\cdot\mathbf{g}(\mathbf{x},t) = 0 \tag{A2}$$

where U ($\mathrm{J\,m^{-3}}$) is the internal energy density and g ($\mathrm{W\,m^{-2}}$) is the energy flux per unit area. If the surface layer is snow, the internal energy density is divided in a water component and an ice component (Zanotti *et al.*, 2004). As a boundary condition of Equation 2, the energy balance at the surface is calculated as (Rigon *et al.*, 2006)

$$R_n + H + LE + G_r = 0 \tag{A3}$$

with the sensible heat flux H ($\mathrm{W\,m^{-2}}$), the latent heat flux LE ($\mathrm{W\,m^{-2}}$) and the soil heat flux G_r ($\mathrm{W\,m^{-2}}$).

Only for the uppermost soil layer is the energy flux g influenced by energy input from precipitation, sensible heat and radiation. The following soil layers are affected only by soil heat flux and evapotranspiration (Rigon *et al.*, 2006). The latter and the dependence of the hydraulic conductivity on temperature together form a strong connection between the water and energy balance.

SOIL HEAT FLUX

The used general equation of the soil heat flux G_r is

$$G_r = -\lambda_s(\mathbf{x},t,\theta)\cdot\frac{\partial T(\mathbf{x},t)}{\partial z} \tag{A4}$$

$\lambda_s(x, t, \theta)$ ($\mathrm{w\,m^{-1}\,K^{-1}}$) is the heat conductivity dependent on the water content θ (—) and the mineral composition of the soil. For the calculation of soil freezing and thawing, the reader is referred to Dall' Amico *et al.* (2011).

SENSIBLE HEAT FLUX

The sensible heat flux H is calculated as (Rigon *et al.*, 2006)

$$H = \rho\cdot c_p\cdot C_H\cdot\hat{u}\cdot\left(T_s - \hat{T}_a\right) \tag{A5}$$

where ρ is the air density ($\mathrm{kg\,m^{-3}}$), c_p is the specific heat ($\mathrm{J\,kg^{-1}\,K^{-1}}$) dependent on the air pressure p ($\mathrm{N\,m^{-2}}$), C_H is the heat transport coefficient (—), $\hat{u}$ is the mean wind velocity ($\mathrm{m\,s^{-1}}$), T_s is the surface temperature and T_s is the air temperature (K).

LATENT HEAT FLUX

Actual evapotranspiration is calculated as a function of potential evapotranspiration E_P ($\mathrm{W\,m^{-2}}$):

$$E_P = \lambda(q(T_s) - q(T_a)\cdot\hat{u}_a)/r_a \tag{A6}$$

with the saturated specific humidity of the air at the surface $q(T_s)$ and at the reference height $q(T_a)$ (—). It is further split into three components:

Evaporation:

$$E_G = (1 - cop)\cdot E_P\cdot\frac{r_a}{r_a + r_s} \tag{A7}$$

where cop (—) is the vegetation cover fraction, E_P is the potential evapotranspiration ($\mathrm{W\,m^{-2}}$), r_a ($\mathrm{s\,m^{-1}}$) is the aerodynamic resistance and r_s is the soil resistance ($\mathrm{s\,m^{-1}}$).

Interception:

$$E_{VC} = cop\cdot E_P\cdot\delta_W \tag{A8}$$

with δ_W being the fraction of wet vegetation (—).

Transpiration:

$$E_{TC} = cop\cdot E_P\cdot(1 - \delta_W)\cdot\Sigma_i^n\cdot\frac{f_{root}^i\cdot r_a}{r_a + r_c^i} \tag{A9}$$

with the portion of roots in every soil layer f_{root}^i (—) and the vegetation resistance r_c^i ($\mathrm{s\,m^{-1}}$) (Della Chiesa *et al.*, 2014). The surface boundary conditions are defined as the conditions of the atmosphere. At the bottom soil layer, the soil temperature follows a sinusoidal change in the annual cycle of temperature. For further details about these routines, the reader is referred to Rigon *et al.* (2006) and Bertoldi *et al.* (2006).

VEGETATION ENERGY BALANCE

The energy balance of the vegetation canopy is calculated according to Endrizzi and Marsh (2010) as

$$C_v\frac{dT_v}{dt} = SW_v + LW_v - H_v - LE_v \tag{A10}$$

with the thermal capacity of vegetation C_v, the time t, shortwave and longwave radiation absorbed by the vegetation SW_v and LW_v and sensible and latent heat flux from the vegetation to the canopy air H_v and LE_v.

WATER BALANCE

To calculate the water balance, a discretized form of the continuity equation is solved, which is true for fluid water at the surface (Rigon *et al*., 2006),

$$\frac{\partial q_{\text{sup}}(x,t)}{\partial t} + c(x,t)\nabla \cdot q_{\text{sup}}(x,t) = c(x,t) \cdot q_{\text{L}}(x,t) \quad \text{(A11)}$$

and in the soil,

$$\frac{\partial \theta(x,t)}{\partial t} + \nabla \cdot q_{sub}(x,t) = -S(x,t) \quad (12)$$

where q_{sup} is the surface runoff per unit area (m s^{-1}), $c(x)$ is the velocity of the kinematic wave varying with space (m s^{-1}), $\nabla \cdot q_{\text{sub}}$ is the water flux divergence per unit volume of soil including horizontal exchange of neighbouring cells described by the Richards equation (see below), q_{L} (s^{-1}) is the unit volume of water exchange with the soil defined positive for infiltration, θ (—) is the volumetric water content of the soil or snow, S (s^{-1}) is the amount of water exchange between the atmosphere and the soil by evaporation and transpiration. For channel and hillslope routing, the reader is referred to Rigon *et al*. (2006). The boundary condition at the bottom can be defined by either horizontal water flows or the conductivity of the bedrock. Surface boundary conditions are treated as in Bixio *et al*. (2000), allowing the infiltration of surface runoff and the exfiltration of subsurface runoff. Subsurface flow of water q_{sub} is calculated using a three-dimensional form of the Richards equation after Paniconi and Putti (1994):

$$q_{\text{sub}} = -K_{\text{s}}(T) \cdot K_{\text{r}}(S_{\text{W}}) \cdot \nabla(\psi + z) \quad (13)$$

where $K_{\text{s}}(T)$ is the saturated hydraulic conductivity (m s^{-1}), taking into account the viscosity of water, which is dependent on temperature T (°C), $K_{\text{r}}(S_{\text{W}})$ is the relative hydraulic conductivity (—), $S_{\text{W}} = \theta/\theta_{\text{s}}$ is the relative water saturation defined as a fraction between the volumetric soil water content θ (—) and the saturated soil water content θ_{s} (—), z is the vertical upward coordinate (m) and ψ is the suction potential (m).

